

This is an electronic reprint of the original article. This reprint may differ from the original in pagination and typographic detail.

Core-Shell Carbon Nanofibers-NiFe Structure on 3D Porous Carbon Foam

Pham, TN; Samikannu, A; Vincze, Z; Zettinig, P; Tesfalidet, S; Wagberg, T; Mikkola, JP

Published in:
Advanced Sustainable Systems

DOI:
[10.1002/adsu.202200310](https://doi.org/10.1002/adsu.202200310)

E-pub ahead of print: 07/11/2022

Document Version
Final published version

Document License
CC BY

[Link to publication](#)

Please cite the original version:

Pham, TN., Samikannu, A., Vincze, Z., Zettinig, P., Tesfalidet, S., Wagberg, T., & Mikkola, JP. (2022). Core-Shell Carbon Nanofibers-NiFe Structure on 3D Porous Carbon Foam: Facilitating a Promising Trajectory toward Decarbonizing Energy Production. *Advanced Sustainable Systems*, Article 2200310. Advance online publication. <https://doi.org/10.1002/adsu.202200310>

General rights

Copyright and moral rights for the publications made accessible in the public portal are retained by the authors and/or other copyright owners and it is a condition of accessing publications that users recognise and abide by the legal requirements associated with these rights.

Take down policy

If you believe that this document breaches copyright please contact us providing details, and we will remove access to the work immediately and investigate your claim.

Core–Shell Carbon Nanofibers-NiFe Structure on 3D Porous Carbon Foam: Facilitating a Promising Trajectory toward Decarbonizing Energy Production

Tung Ngoc Pham,* Ajaikumar Samikannu, Zsuzsanna Vincze, Peter Zettinig, Solomon Tesfalidet, Thomas Wågberg, and Jyri-Pekka Mikkola*

In this work, a low-cost, light-weight, highly efficient, and durable electrode in which NiFe-layered double hydroxide is electrodeposited on a carbon nanofiber (CNF) core supported on a carbon foam (CF) is introduced. The resulting 3D NiFe-CNFs-CF electrode shows excellent oxygen evolution reaction and hydrogen evolution reaction performance in alkaline media. When used as an anode and a cathode in the same cell, a current density of 10 mA cm^{-2} is achieved, at a cell voltage of 1.65 V. Moreover, good stability over a long testing time (50 h) is demonstrated. The ternary hybrid electrode gives rise to an excellent performance-to-weight ratio owing to its very low bulk density ($\approx 34 \text{ mg cm}^{-3}$) inherited from super lightweight components composed of CF and CNFs. The developed electrode can potentially be used in large-scale alkaline water electrolysis, in facilities such as offshore hydrogen production platforms, which can complement the variable renewable energy production of wind farms through hydrogen storage and fuel cells.

technological developments have practical implications to solve the bigger quandary of decarbonizing energy production. Water electrolysis is one of the most attractive methods used to produce hydrogen, which is widely accepted as an excellent alternative to the traditional nonrenewable energy sources or fossil fuels.^[1–3] For hydrogen production, renewable energy resources such as solar, wind, and wave energy are used to power electrolysis at offshore locations to utilize abundant resources.^[4,5] A highly suitable application for water electrolysis systems would be coupling them with offshore wind energy generation to establish viability and increase effectiveness of components by combining these technologies to create system level innovations, which contribute to decarbonizing the world economy.

1. Introduction

The primary aim of the paper is to report the results of experiments with catalyst-electrode development for water splitting. The paper also provides multidisciplinary reflections on how

In the electrolysis of water, hydrogen is generated at the cathode through the hydrogen evolution reaction (HER) and oxygen is evolving at the anode through the oxygen evolution reaction (OER) under an applied potential^[6,7] which is always higher than the theoretical value of 1.23 V. In alkaline water

T. N. Pham
Department of Chemistry
The University of Danang
University of Science and Technology
54 Nguyen Luong Bang, Lien Chieu, Da Nang 550000, Vietnam
E-mail: pntung@dut.udn.vn

A. Samikannu, S. Tesfalidet, J.-P. Mikkola
Technical Chemistry
Department of Chemistry
Chemical-Biological Centre
Umeå University
Umeå SE-90187, Sweden
E-mail: jyri-pekka.mikkola@umu.se

Z. Vincze
Entrepreneurship
Umeå School of Business
Economics and Statistics
Umeå University
Umeå SE-90187, Sweden

P. Zettinig
International Business
Department of Marketing and International Business
University of Turku
Turku FI-20500, Finland

T. Wågberg
Department of Physics
Umeå University
Umeå SE-90187, Sweden

J.-P. Mikkola
Industrial Chemistry & Reaction Engineering
Department of Chemical Engineering
Process Chemistry Centre
Åbo Akademi University
Åbo-Turku FI-20500, Finland

 The ORCID identification number(s) for the author(s) of this article can be found under <https://doi.org/10.1002/adsu.202200310>.

© 2022 The Authors. Advanced Sustainable Systems published by Wiley-VCH GmbH. This is an open access article under the terms of the Creative Commons Attribution-NonCommercial License, which permits use, distribution and reproduction in any medium, provided the original work is properly cited and is not used for commercial purposes.

DOI: 10.1002/adsu.202200310

electrolysis, the exceeding over-potential is mainly caused by the high activation barrier of the electrode materials and the total ohmic resistance in the electrochemical cell.^[8] Therefore, in order to minimize the over-potential and enhance the efficacy of the process, an effective electrocatalyst should be employed.

Noble metal-based catalysts such as IrO₂/RuO₂ and Pt are benchmark electrocatalysts for OER and HER, respectively, owing to their small onset potential.^[9–11] However, the high cost and the shortage of these precious metals create economic pressure and subsequently prevent them from large-scale application. Hence, electrocatalysts based on nonprecious and earth-abundant materials have been proposed as viable alternatives to the noble metal catalysts. Recently, it has been revealed that earth-abundant materials such as metal oxides/hydroxides,^[6,12–18] metal chalcogenides,^[19–22] and pnictogenides^[23–26] possess high electrocatalytic activity in the water-splitting reaction. Especially, despite the common sense that a catalyst which is active for OER may exhibit a sluggish activity toward HER and vice versa, some of these materials have been proven to work efficiently as bifunctional catalysts with good activity for both OER and HER.^[14,15,23,24,27–29] Among these bifunctional catalysts, due to its low cost, special structure, and high catalytic activity, NiFe-layered double hydroxide (NiFe LDH) is probably one of the most promising catalysts to be employed in overall water electrolysis.^[14,15,27] The NiFe LDH can be easily synthesized through either hydrothermal method^[14,28] or by electro-deposition^[15,30] of which the latter is fast, simple, and easy to scale-up.

Besides the catalyst, the electrode matrix/substrate is also an important factor to promote the catalytic performance of the electrode. Recently, 3D structured electrodes fabricated from conductive materials such as nickel foam and copper foam have received much attention from scientists owing to their large surface area, easy dissipation of the generated gas bubbles as well as rapid and unhindered penetration of electrolytes into the whole electrode matrix.^[15,30–32] Also, to further increase the surface area and thus promote the overall catalytic activity, nanostructures were grown directly on such foams, e.g., CuO and CuCO₂S nanowires on copper foam^[15,21,33] and Ni nano-chains, CuCoO_x, NiSe, and ZnO nanowires/nanorods on nickel foam.^[16,17,22,34] Based on these special design structures, a 3D core–shell-structured NiFe LDHs can be synthesized^[15,34] which, in turn, acts as a very efficient catalyst for the overall water-splitting reaction. However, these excellent materials bear a major disadvantage due to their complex and high energy demanding manufacturing procedure^[35,36] where the expense can limit their use in large-scale applications.

Because of their well-known advantages related to their high chemical stability, light-weight structure, low price, and the possibility to recover the metal catalysts, carbon materials such as carbon cloth (CC),^[37,38] carbon fiber paper (CFP),^[27,39,40] and glassy carbon^[41,42] have been widely studied as electrode matrix in the electrochemical water-splitting studies. Decoration of the surface of carbon materials with graphene and carbon nanotubes (CNTs) has also been used to boost the surface area and subsequently increase their performance to a level which is comparable to metal foam materials.^[12,28,41,43] However, the bulk density of the CFP and CC which is in the order of 450 and 380 mg cm⁻³,^[44] respectively, is similar to those of metal

foams which can reach values as low as 400 and 450 mg cm⁻³ for copper foam and nickel foam, respectively.^[30,45] Thus, the performance-to-weight ratio of electrodes based on CFP and CC is not superior to metal foam-based electrodes and cannot be introduced as outstanding candidates for offshore facilities where the weight is one of the limiting factors.

Herein, we introduce NiFe LDH decorated on carbon nanofibers-carbon foam (NiFe-CNFs-CF) electrode with a 3D porous core–shell structure. The NiFe-CNFs-CF combines the advantages of different materials: low price and extremely low bulk density of the melamine foam^[46] and CF, high surface area, electrical conductivity, and chemical resistance of CNFs as well as the excellent catalytic activity of the NiFe LDH catalyst. The electrode, as prepared, possesses high catalytic activity and excellent durability which is comparable with the “state-of-the-art” reported catalyst for both OER and HER. For the overall water splitting, in the two-electrode setup, the NiFe-CNFs-CF also showed a good performance, operating with a cell potential of only 1.65 V to reach the current density of 10 mA cm⁻², and good stability after a long-running time (50 h) at 10 mA cm⁻². Due to the extremely low bulk density of the electrode (≈34 mg cm⁻³), the performance-to-weight ratio of the NiFe-CNFs-CF electrode is surprisingly high and reached the specific current of 10 A g⁻¹, at the over-potential of 240 and 130 mV for OER and HER, respectively. The NiFe-CNFs-CF electrode can be synthesized using simple and scalable methods such as pyrolysis, catalytic chemical vapor deposition (CCVD), and electrodeposition, and as such the CF electrode has the potential to be used in a large-scale alkaline water electrolysis, especially in offshore facilities.

2. Results and Discussions

2.1. Material Characterization

The morphology, as well as the nanostructure of prepared samples, was investigated by scanning electron microscopy (SEM). At low magnification, **Figure 1a** shows the 3D structure of the CF with an open-cell structure and, at a higher magnification, a smooth surface (**Figure S3a**, Supporting Information). The SEM image of the CF after the CCVD process (**Figure 1b,c** and **Figure S3b**, Supporting Information) shows a dense mat of short and curved CNFs entangled into spaghetti-like form, which completely covers the surface of the CF. The presence of CNFs and a small portion of CNTs was confirmed by the transmission electron microscopy (TEM) image (**Figure S4**, Supporting Information) where a combination of both CNFs and CNTs on the surface of the CF is shown. However, only CNFs are mentioned in the name of the material (CNFs-CF) for the sake of simplification. The high-resolution TEM (HRTEM) images reveal that the CNFs are in the amorphous form where a very little crystalline structure was found on the image (**Figure S5a,b**, Supporting Information). The presence of these carbon nanostructures can also be recognized through the rise of the bulk density (**Figure S6**, Supporting Information) which is increased from 9 (±0.5) for CF to 18 (±1) mg cm⁻³ for CNFs-CF, with a concurrent increase of the specific surface area of the material after the CCVD process. The Brunauer–Emmett–Teller (BET)

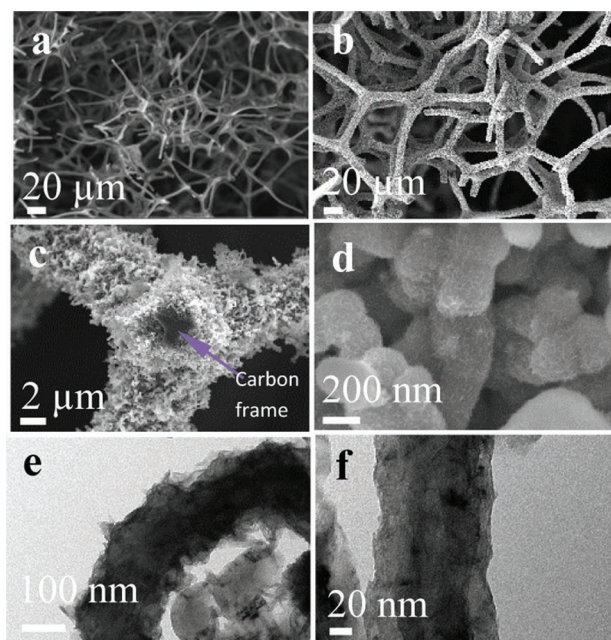


Figure 1. SEM images at different magnifications of a) CF, b) low, and c) high magnification of CNFs-CF and d) NiFe-CNFs-CF at high magnification. TEM images of e) CNFs and d) CNTs shelled with NiFe catalyst of NiFe-CNFs-CF sample.

surface area based on the N_2 sorption–desorption isotherm was calculated to be $\approx 46 \text{ m}^2 \text{ g}^{-1}$, which is ten times bigger than that of the CF alone ($4 \text{ m}^2 \text{ g}^{-1}$).

Ni and NiFe catalysts were deposited onto the CF and CNFs-CF substrates by electrodeposition leading to the formation of electrodes denoted as Ni-CF, NiFe-CF, Ni-CNFs-CF, and NiFe-CNFs-CF. Figure 1d and Figures S7–S9 in the Supporting Information reveal that catalyst morphology on survey electrodes is strongly affected by the type of catalyst employed and by the presence of CNFs on the electrode substrate. The SEM images of the Ni-CF electrode (Figure S7, Supporting Information) showed the presence of particles or aggregates with sizes ranging from 150 to 200 nm of nickel catalyst on the CF surface, which is completely different from the thick film found on the surface of the NiFe-CF electrode (Figure S8, Supporting Information). In the case of CNFs-CF substrate, the obtained catalyst morphology was also found to be very distinctive in which a nickel film was found on the surface of Ni-CNFs-CF (Figure S9, Supporting Information) and nanosheet like structures were observed on the surface of the NiFe-CNFs-CF (Figure 1d). Remarkably, the TEM images of NiFe-CNFs-CF showed different catalyst morphology for CNFs and CNTs. While the CNFs are completely covered by ultrathin nanosheets forming a highly porous core–shell structure (Figure 1e and Figure S5c,d, Supporting Information), a thin film (around 20 nm) is formed on the surface of CNTs (Figure 1f) after the electrodeposition process. The energy dispersive X-ray spectroscopy (EDS) mapping analysis of NiFe-CNFs-CF (Figure 2) where carbon, nickel, and iron were indexed in yellow, blue, and purple colors, respectively, showed the symmetric distribution of Ni and Fe on the carbon frame. To identify the catalyst loading of the NiFe-CNFs-CF, thermal gravimetric analysis

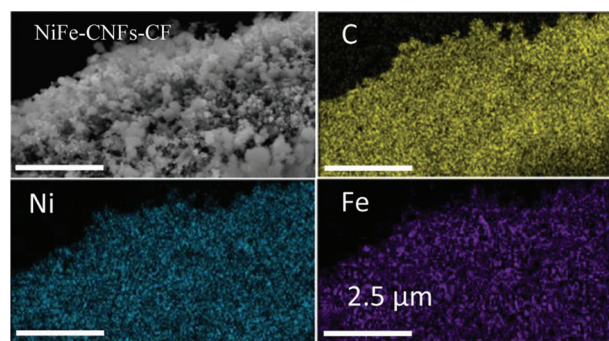


Figure 2. SEM-EDS image of the NiFe-CNFs-CF with the corresponding elemental mapping.

(TGA) measurement was carried out. The TGA showed a catalyst loading at around 15 wt% (Figure S10, Supporting Information). The result was further confirmed by inductively coupled plasma-optical emission spectroscopy (ICP-OES) analysis of the digested NiFe-CNFs-CF sample which gave a similar amount of catalyst loading ($\approx 14 \text{ wt}\%$). Due to the very low density of CNFs-CF, even at 15 wt% of catalyst loading, the NiFe-CNFs-CF sample that has a geometric area of 1 cm^2 contains an extremely small amount of metal catalysts ($\approx 0.37 \text{ mg}$).

To identify the phase of samples such as CF, CNFs-CF, and NiFe-CNFs-CF, the X-ray diffraction (XRD) was carried out. As shown in Figure 3a, compared with the amorphous CF, the XRD pattern of the CNFs-CF sample showed the presence of peaks at the 2θ of 26.4° and 44.0° which can be assigned as graphite and thus further confirm the formation of ordered carbon structures, i.e., CNTs.^[47] At the same time, the presence of cobalt which was used as a catalyst in the CCVD process was also revealed through a small peak located at 51.5° .^[48] Compared with CNFs-CF, the XRD pattern of NiFe-CNFs-CF samples exhibited several new diffraction peaks found at 11.5° , 34.5° , 60.7° , and also a peak at $\approx 23.2^\circ$ (overlapped by the nearby graphite peak) which can be characterized as NiFe LDH.^[12,49] The weak signals of these peaks also suggest that the majority of NiFe catalyst can be in the amorphous form.^[49,50] The speculation is confirmed by the HRTEM image of the NiFe-CNFs-CF (Figure S5d, Supporting Information) where no ordered structure was found on the catalyst. The composition, as well as the oxidation stage of the NiFe-CNFs-CF catalyst, was further investigated by X-ray photoelectron spectroscopy (XPS). The wide spectra of samples taken at the inner and outer layer of NiFe-CNFs-CF are similar and show the presence of carbon, oxygen, nickel, and iron on the surface of the sample (Figure S11, Supporting Information). Furthermore, impurity elements such as S and Cl which do not come from the CNFs-CF surface^[18] but probably from trapped metal precursors were also found on the surface of the electrode. The high homogeneity of the deposited catalyst on the outer layer and the inner layer of the electrode was also confirmed where a similar Ni/Fe atomic ratio between the outer and inner layer (2.8/1 and 2.6/1, respectively) was found. In conclusion, the average atomic ratio of Ni/Fe is estimated to be 2.7/1 which is lower than the molar ratio of Ni/Fe used in the plating bath (5/1). Moreover, the atomic ratio of Ni/Fe derived from EDS spectra (Figure S12, Supporting Information) of NiFe-CNFs-CF (around 3.1/1) is in

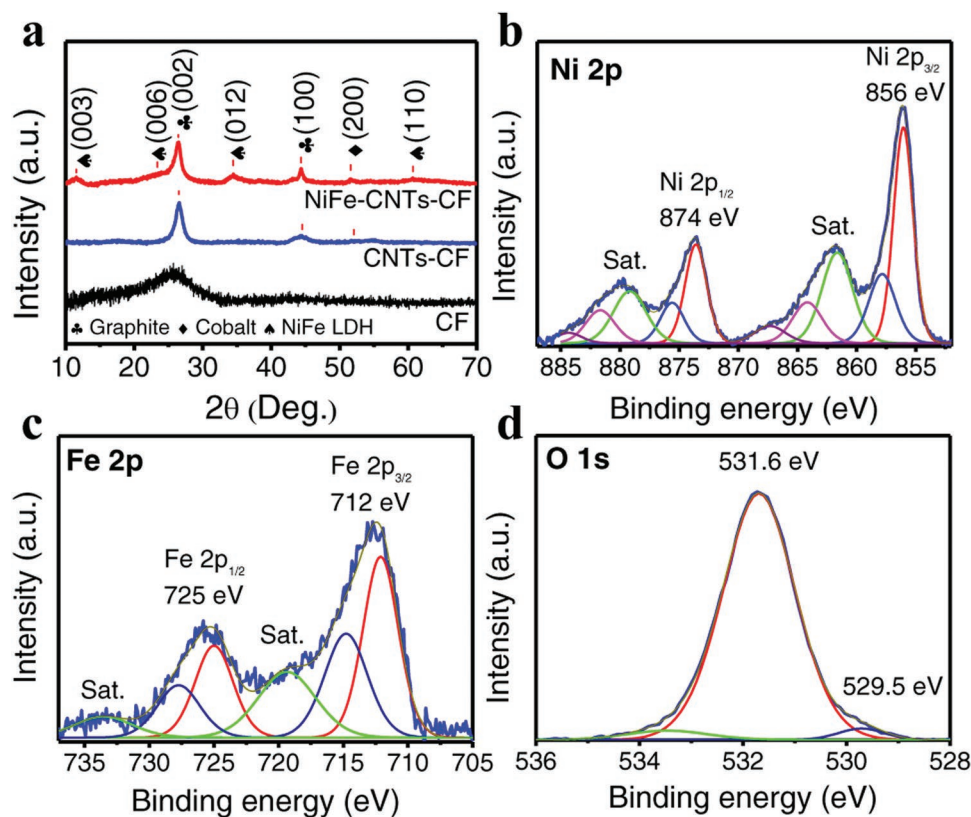


Figure 3. a) XRD pattern of CF, CNFs-CF, and NiFe-CNFs-CF. High-resolution XPS spectra of b) Ni 2p, c) Fe 2p, and d) O 1s of NiFe-CNFs-CF.

agreement with the XPS results. The results suggest that the deposition rate of iron was faster than that of nickel which is similar to the conclusion of Torabinejad and his co-worker that the co-electrodeposition of nickel and iron from an electrolyte is an anomalous deposition.^[51] The oxidation stage of Ni and Fe on the surface of CNFs-CF was also revealed by XPS. As shown in the Ni 2p spectrum (Figure 3b), two main peaks at 856 eV (Ni 2p_{3/2}) and 874 eV (Ni 2p_{1/2}) and two shakeup satellite peaks indicate the presence of Ni²⁺ in the sample.^[13,52] On the other hand, the absence of the Ni 2p_{3/2} peak at around 852 eV also implies that there is no evidence of the existence of Ni metal in the sample.^[53] The oxidation stage of iron in the NiFe-CNFs-CF sample was identified through the Fe 2p high-resolution spectrum (Figure 3c). The peaks at 725 eV (Fe 2p_{1/2}), 712 eV (Fe 2p_{3/2}), and the shakeup satellite peak at around 719.5 eV entailed that a major amount of iron in the sample surface is in the trivalent stage.^[30,54] Additionally, the O 1s high-resolution spectrum (Figure 3d) showed a dominant peak at 531.6 eV which can be characterized as the metal-bound hydroxide group (M–OH), and a small peak at 529.5 eV which represents metal-bound oxygen (M=O). These findings confirm that a major part of Ni and Fe exits in their respective hydroxide form rather than their oxide form. It is worth noting that there is no difference in the oxidation stage of Ni and Fe between the inner and the outer layer of the NiFe-CNFs-CF electrode where the high-resolution spectra of Ni 2p and Fe 2p of these samples showed a very similar pattern (Figure S9b,c, Supporting Information).

2.2. Electrochemical Performance

2.2.1. The OER Performance

The OER activity of different catalysts, e.g., NiFe-CNFs-CF, Ni-CNFs-CF, NiFe-CF, Ni-CF, and the blank CNFs-CF was explored by polarization scan at a scan rate of 5 mV s⁻¹ in 1.0 M KOH electrolyte. As shown in **Figure 4a**, due to its high hydrophobicity, the blank electrode (CNFs-CF) exhibits a negligible activity compared with other metal catalyst-decorated electrodes. As a result, the contribution of the electrode substrate (CNFs-CF) to the OER activity is negligible. On the other hand, the NiFe-CNFs-CF outperformed other electrodes since it requires a very low over-potential (η) of 245 and 328 mV to reach the current density (j) of 10 and 100 mA cm⁻², respectively. It is worth noting that to eliminate the influence of the oxidation peak of nickel (≈ 1.4 V vs reversible hydrogen electrode (RHE)), although the estimated over-potential values were identified based on the backward cyclic voltammetry (CV) scan, these values are still comparable with the reported “state-of-the-art” catalysts using transition metal oxides/hydroxides as well as metal-doped nonmetal elements (Table S1, Supporting Information). Through OER polarization scans, the superiority of the NiFe LDH co-catalyst over Ni catalyst can be seen clearly from their onset potential where the onset potential of NiFe-decorated electrodes (NiFe-CNF-CF and NiFe-CF) (≈ 1.45 V vs RHE) is lower than that of Ni-CNFs-CF and Ni-CF electrodes (≈ 1.57 V vs RHE) (Figure S13, Supporting Information).

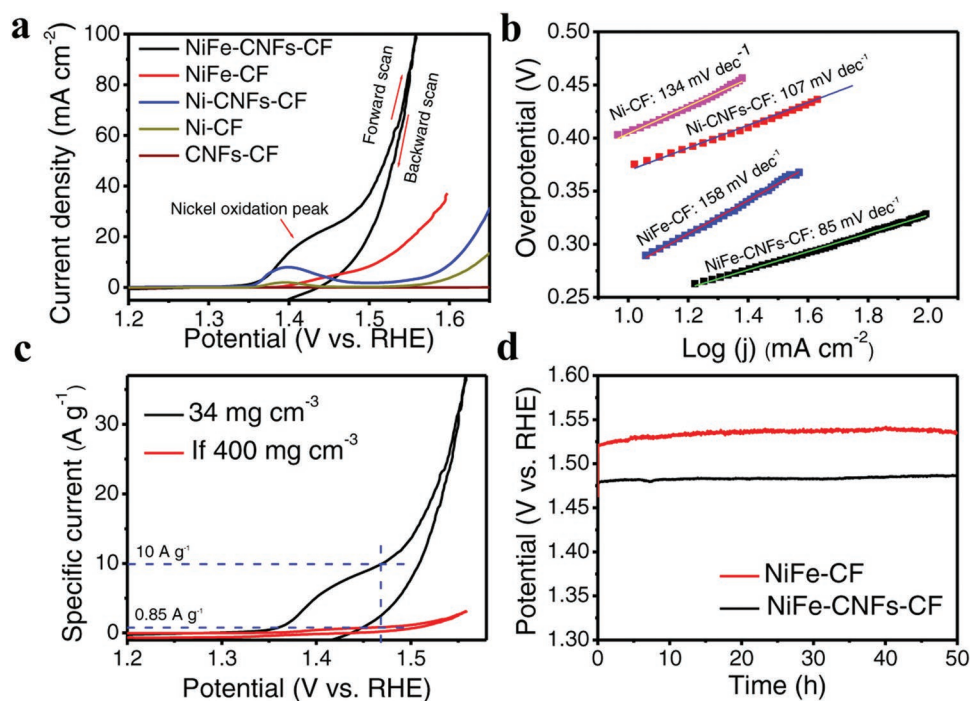


Figure 4. a) Polarization curves at the scan rate of 5 mV s^{-1} and b) corresponding Tafel plots of Ni-CF, NiFe-CF, CNFs-CF, Ni-CNFs-CF, and NiFe-CNFs-CF electrodes. c) The OER specific current of NiFe-CNFs-CF electrode at the bulk density of 34 mg cm^{-3} and the reference bulk density value of 400 mg cm^{-3} . d) Chronopotentiometry curves of NiFe-CF and NiFe-CNFs-CF electrodes at the current density of 10 mA cm^{-2} . All of the experiments were performed in 1 M KOH electrolyte.

Additionally, as can be seen from Tafel plots (Figure 4b), CNFs-CF-based electrodes always show a smaller Tafel slope than that of CF-based electrodes. For example, the NiFe-CNFs-CF electrode exhibits the smallest Tafel slope (85 mV dec^{-1}) followed by Ni-CNFs-CF (107 mV dec^{-1}), Ni-CF (134 mV dec^{-1}), and NiFe-CF (158 mV dec^{-1}). The result indicates that due to their highly arranged graphene layer structures, CNFs (and CNTs) facilitate the electron transport and thus enhance the catalytic activity of the hybrid CNF-CF electrodes. Thus, we can conclude that the excellent OER activity of the NiFe-CNFs-CF electrode was brought by the excellent catalytic activity of the NiFe LDH catalyst as well as the high electrical conductivity and high surface area of CNFs grown directly on the CF surface.

Furthermore, the clues for the high OER activity of the NiFe-CNFs-CF electrode can be seen through the double-layer capacitance (C_{dl} , Figure S14, Supporting Information) which is proportional to the electrochemically active surface area (ECSA). Compared with other electrodes, the CNFs-CF blank electrode showed a very small C_{dl} of only 0.5 mF cm^{-2} , owing to its high hydrophobicity. On the other hand, due to the presence of the unique nanostructures of the NiFe LDH catalyst, the C_{dl} of the NiFe-CNFs-CF electrode was calculated to be around 21.1 mF cm^{-2} which by far higher than that of Ni-CF (13 mF cm^{-2}), Ni-CNFs-CF (12.6 mF cm^{-2}), and NiFe-CF electrode (10.2 mF cm^{-2}). The high ECSA value of the NiFe-CNFs-CF electrode reveals that the material contains a lot of active sites for the catalytic reaction which in turn well explains its excellent performance toward OER and the high HER activity (see the HER section).

The stability of the NiFe-CNTs-CF and the NiFe-CF electrodes was investigated by chronopotentiometry, at a constant current of 10 mA cm^{-2} in 1 M KOH solution. As shown in Figure 4d, the NiFe-CNTs-CF electrode exhibits excellent durability with almost no obvious increase of the over-potential after a long testing time (50 h). On the other hand, the NiFe-CF electrode was a bit less stable during the stability test where the measured over-potential showed a slight increase during the first 30 h, followed by a decrease after 40 h which might indicate not a better OER catalytic activity but oxidation/corrosion of the carbon electrode. To identify the problem, a UV-Vis scan (200–800 nm) was used to analyze the electrolyte after the stability test of NiFe-CF and NiFe-CNFs-CF electrodes. As shown in Figure S15 in the Supporting Information, for the NiFe-CF electrode, there is an intense peak at the UV region (with a shoulder peak at around 300 nm) on the absorbance spectra of the electrolyte after the stability test. The peak could be characterized as the signal of soluble organic compounds caused by the corrosion of carbon during the OER.^[55] It is worth noting that in the case of the NiFe-CNFs-CF electrode, after the chronopotentiometry test, a much smaller peak at the same wavelength was observed suggesting that the corrosion rate of carbon is negligible. The result indicates that the presence of CNFs on the electrode surface brought not only a higher OER performance but also better stability for the electrode.

The leaching of nickel and iron catalyst during the stability test of the NiFe-CNFs-CF electrode was identified by using ICP-OES to measure the electrolyte sample taken after the test (50 h). The ICP-OES result showed that while only a tiny

concentration of iron (0.06 ppm) was found in the electrolyte, the concentration of nickel ion was under the detection limit of the instrument. It is worth noting that the total amount of iron was calculated to be just around 0.4 μg in total. The result from the leaching test indicated corrosion of iron but at a very low level during the stability test. The morphology of the NiFe catalyst after the stability test was also investigated using the SEM technique. As shown in the SEM image (Figure S16, Supporting Information), no corrosion mark was observed and the unique nanostructure of the NiFe LDH catalyst has remained. Thus, the obtained results further confirm the excellent stability of the NiFe-CNFs-CF electrode in OER.

2.2.2. The HER Performance

To investigate the possibility of our 3D NiFe-CNFs-CF catalyst for overall water splitting, we examined the HER activity of the foam electrodes in 1 M KOH. Among the prepared electrodes, the NiFe-CNFs-CF exhibits the best electro-catalytic performance showing an extremely low over-potential of 70 and 230 mV, at the current density of -10 and -100 mA cm^{-2} , respectively (Figure 5a) and also the lowest Tafel slope (139 mV dec^{-1}) (Figure S17a, Supporting Information). The obtained results show that our catalyst has equally good catalytic performance with recently reported catalysts which are presented in Table S2 in the Supporting Information. It is worth noting that the high HER catalytic activity of the NiFe-CNFs-CF is brought by the NiFe LDH catalyst where the blank, CNFs-CF, electrode showed no HER activity at the same testing condition (Figure 5a).

Remarkably, the difference between investigated electrodes is small as other electrodes also showed a decent to good HER performance. For example, the Ni-CNFs-CF electrode exhibited a good catalytic activity which needs only 100 and 280 mV of over-potential to reach the current density of -10 and -100 mA cm^{-2} , respectively, which is on par with other “state-of-the-art” catalysts. Despite having the lowest catalytic activity among our prepared electrodes, the Ni-CF electrode still showed a decent HER performance which is far better than the Ni foam itself.^[32] These results are very promising and open up for further research focusing on the potential to use the CF-decorated nickel catalyst electrode as the cathode in the alkaline water-splitting process.

As depicted in Figure 5b, the stability of the NiFe-CNFs-CF was evaluated by chronopotentiometry tests performed at high current density, i.e., -50 and -150 mA cm^{-2} , in 1 M KOH electrolyte. The electrode showed no degradation after 100 h, at a current density of -50 mA cm^{-2} and only a small increase in the over-potential ($\approx 25 \text{ mV}$) was observed at a high current density of -150 mA cm^{-2} after 100 h. To explain the excellent stability of the NiFe-CNFs-CF electrode, ICP-OES was used to measure the leaching amount as well as the leaching rate of Ni and Fe during the stability test (100 h at -150 mA cm^{-2}). After the first hour, around 0.41 ppm of iron and 0.02 ppm of nickel equal to the amount of 2.5 and 0.1 μg of iron and nickel, respectively, were found in the electrolyte (Figure S17b, Supporting Information). Surprisingly, the ICP-OES result of the sample taken after 100 h showed a small amount of iron ($\approx 0.14 \text{ ppm}$ or 1 μg) and no detectable amount of nickel. The results revealed a faster rate of corrosion at the beginning which slowed down

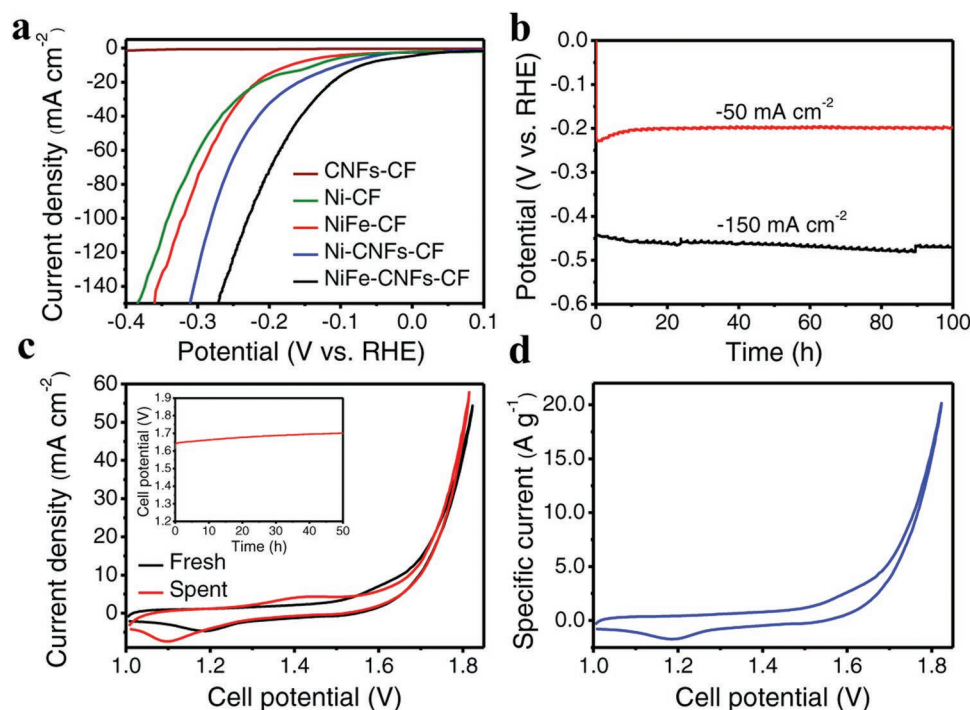


Figure 5. a) Polarization curves of Ni-CF, NiFe-CF, CNFs-CF, Ni-CNFs-CF, and NiFe-CNFs-CF electrodes. b) Chronopotentiometry curves of NiFe-CNFs-CF electrode at the high HER current density of -50 and -150 mA cm^{-2} . c) The CVs of the NiFe-CNFs-CF before (fresh) and after (spent) the stability test using a two electrodes setup (inset: the chronopotentiometry curve of NiFe-CNFs-CF cell in the stability test at the constant current density of 10 mA cm^{-2}). d) The specific current of NiFe-CNFs-CF//NiFe-CNFs-CF. All of the experiments were performed in 1 M KOH electrolyte.

during the remaining period of the stability test. It seems that the small corrosion, which was calculated to be 3.5 μg of iron and 0.1 μg of nickel in total, has a negligible effect on the catalyst morphology where the SEM image of the sample after the stability test (Figure S18, Supporting Information) showed no sign of corrosion nor change in the catalyst morphology after the lengthy stability test.

2.2.3. Turn Over Frequency

The efficiency of the NiFe catalyst was examined through the turnover frequency (TOF) which was calculated based on the total amount of catalyst loading and the corresponding polarization curves of OER and HER. For OER, the TOF at the overpotential (η) of 350 mV is 0.034 s^{-1} which is comparable with other “state-of-the-art” NiFe catalysts such as Janus Ni-Fe nanoparticles (0.052 s^{-1} , at the same η)^[27] and NiFe/NF (0.075 s^{-1} , at $\eta = 400\text{ mV}$).^[30] In the case of HER, the TOFs at the overpotential of 200 and 250 mV are 0.030 and 0.051 s^{-1} , respectively, values which are a bit lower than other nonprecious benchmark catalysts such as Ni-Fe NPs (0.056 s^{-1})^[27] and Mo_2N (0.07 s^{-1} , at $\eta = 250\text{ mV}$).^[56] It is worth noting that because only the top atomic layer of the $\approx 20\text{ nm}$ thickness NiFe LDH film (Figure 1e,f) is active during the HER, the use of the total amount of catalyst for TOF calculation results leads to an extreme underestimation of the TOF value of our catalyst.

2.2.4. The Overall Water Splitting

The overall performance of the NiFe-CNFs-CF electrode for the splitting of water was evaluated by using the same electrode as both anode and cathode in a two-electrode setup in 1 M KOH (Figure S19a, Supporting Information). From the recorded CVs (Figure 5c), the overall water-splitting using NiFe-CNFs-CF required only a low cell potential of 1.65 V to reach the current density of 10 mA cm^{-2} which is a bit higher than some other metal-based electrode systems but similar to other “state-of-the-art” carbon-based electrodes (Table S3, Supporting Information). The stability test, performed at a constant current density of 10 mA cm^{-2} , exhibits good stability after 50 h (Figure 5c, inset). As shown in Figure 5c, the catalytic performance of the NiFe-CNFs-CF cell remained unchanged after the stability test which further confirms the good stability of the electrodes. The NiFe-CNFs-CF showed a very high and stable Faradaic efficiency for HER, which is close to 100%, after a long testing time (50 h). The faradaic efficiency of OER at the anode is also high ($>90\%$) and stable after 50 h at the constant current density of 10 mA cm^{-2} (Figure S19b, Supporting Information). Again, ICP-OES and XPS techniques were employed as complementary techniques to evaluate the stability of the electrode. The ICP-OES measurements made on the electrolyte sample taken after the stability test showed a negligible amount (0.04 ppm, 0.3 μg in total) of iron and no sign of nickel, which is similar to the results from the leaching test in OER. This confirms the excellent stability of the NiFe-CNFs-CF, used as electrode material for both the anode and the cathode, in the two-electrode setup. Moreover, after the stability test, the elemental composition, as well as

the oxidation stage of the NiFe-CNFs-CF electrodes (anode and cathode), were carefully investigated using the XPS technique. As shown in Figure S20 in the Supporting Information, the wide spectra of anode and cathode samples are identical, showing the presence of Ni, Fe, C, and O elements. The presence of a small amount of potassium as an impurity, which can be due to the adsorption of K ions from the electrolyte onto the surface of the electrodes, was also found on both the anode and the cathode. The high-resolution spectra of Ni 2p, Fe 2p, O 1s, and C 1s (Figure S20b–d, Supporting Information) of the spent anode and cathode showed the same shape as the fresh electrode suggesting that the oxidation stage of Ni and Fe catalysts did not change after the stability test. These results reveal the good stability of the NiFe-CNFs-CF electrode using as both anode and cathode in the overall water-splitting experiment.

2.2.5. The Performance-to-Weight Ratio

To evaluate the importance of the weight of the electrode, the specific current (A g^{-1}) was calculated by dividing current density (A cm^{-2}) by the whole weight of the electrode (g cm^{-2}). For comparison purposes, a reference specific current was fabricated assuming the CF has the same density as the copper foam (400 mg cm^{-3}).^[45] Due to the extremely low bulk density of the CNFs-CF substrate ($\approx 18\text{ mg cm}^{-3}$) and a low catalyst loading (15 wt%), the electrode possesses an impressive specific current where only low overpotentials of 240 and 130 mV are required to deliver a current of 10 A g^{-1} during OER and HER, respectively (Figure 4c and Figure S17c, Supporting Information). As can be seen from these figures, if the NiFe-CNFs-CF electrode has the same bulk density as the copper foam, a much lower value of specific current (0.85 A g^{-1} which is nearly 12 times smaller than that of the low bulk density NiFe-CNFs-CF electrode $\approx 34\text{ mg cm}^{-3}$) was achieved at the same potential. When the NiFe-CNFs-CF were used as both anode and cathode in a two-electrode configuration, it required only a cell voltage of $\approx 1.75\text{ V}$ to reach the specific current of 10 A g^{-1} (Figure 5d). Thus, the low density of our CF electrode could be considered as one of the most important advantages of our NiFe-CNFs-CF electrode as well as the CNFs-CF material comparing with other well-documented 3D materials, especially metal foams which have a much higher bulk density.^[30,45]

3. Conclusions

In this work, we have developed a unique NiFe-CNFs-CF electrode which is based on CNFs shelled with NiFe LDH nanosheet structure which plays a key role in the water-splitting reactions on 3D porous CF. The important features which the electrode combines include very light-weight, high surface area, excellent durability, and high catalytic activity. The electrode showed not only an excellent performance toward OER but also high HER performance in an alkaline electrolyte which allows the electrode to be used as efficient material in the overall water splitting. Moreover, the electrode showed an excellent performance to weight ratio which can be considered as a major advantage of the CF electrode over other traditional materials. In general,

the ternary hybrid electrode, which was synthesized through simple (pyrolysis and CCVD) and very fast (electrodeposition) procedures, has the potential to be implemented in large-scale alkaline water-splitting systems. The NiFe-CNfS-CF is probably one of the most promising electrodes to be employed in overall water electrolysis due to its low cost, effective structural properties for high catalytic activity.

4. Experimental Section

Materials: Melamine foam (Basotect G) was purchased from BASF. Cobalt (II) acetate tetrahydrate ($\text{Co}(\text{C}_2\text{H}_3\text{O}_2)_2 \cdot 4\text{H}_2\text{O}$), nickel (II) sulfate hexahydrate ($\text{Ni}(\text{SO}_4)_2 \cdot 6\text{H}_2\text{O}$), nickel (II) chloride hexahydrate ($\text{NiCl}_2 \cdot 6\text{H}_2\text{O}$), iron (III) nitrate nonahydrate ($\text{Fe}(\text{NO}_3)_3 \cdot 9\text{H}_2\text{O}$), and thiophene ($\text{C}_4\text{H}_4\text{S}$, 99%) were purchased from Sigma Aldrich. Dimethylformamide (DMF) was purchased from VWR. Silver paint and carbon glue were purchased from PELCO. Nafion N117 membrane was bought from Ion Power. All chemicals were used as received.

Synthesis of CF: The electrically conductive CF sample (denoted as CF) was synthesized following the procedure described in our previous work.^[18] Briefly, melamine-based polymer foam (BASF, Basotect G, used as received) was pyrolyzed at 900 °C (6 h, the ramping rate of 5 °C min⁻¹) in a quartz reactor under N₂ flow (50 mL min⁻¹). After completion, the system was allowed to cool to RT under an inert (nitrogen) atmosphere. Finally, the synthesized CF was washed several times by water and then dried at 80 °C in air, overnight. A picture showing both the melamine foam and CF is presented in Figure S1a in the Supporting Information.

Synthesis of CNfS-CF: In a typical procedure, 20 mg of cobalt (II) acetate tetrahydrate was dissolved in 2 mL of DMF and sonicated for 3 min. Thereafter, 65 μL of thiophene was added to the mixture and stirred vigorously for 5 min. In the next step, 30 min after the addition of the CF sample (≈20 mg), the solvent was evaporated at 125 °C under nitrogen flow, leaving the cobalt catalyst on the surface of CF. CNfS were grown on the CF substrate utilizing CCVD. The sample was placed on a quartz boat which then was inserted into a horizontal quartz tube. The system was purged with the Varigon gas (5% hydrogen in argon gas, 180 mL min⁻¹) for 20 min and then heated to 670 °C with 20 min heating time. After reaching the anticipated temperature (670 °C), acetylene was introduced into the system at a flow rate of ≈3.8 mL min⁻¹ for 30 min while keeping the Varigon gas flow at the same flow rate. Finally, the system was allowed to cool down to RT under argon gas flow (180 mL min⁻¹).

Synthesis of Catalyst Materials: To prepare electrodes, the CF samples (CF or CNfS-CF) were cut to an appropriate thickness (≈1.6 mm) using a surgical blade. A copper wire was attached to an electrode material using the silver paste and allowed to dry overnight. For the anode, carbon glue was used to cover the silver paste to avoid the oxidation of silver during OER. Before the electrodeposition, CF electrodes were pre-wetted by ethanol 96% and then impregnated in the plating solution to remove ethanol. The electrodeposition was carried out in a standard three-electrode system containing CNfS-CF or CF as the working electrode, a platinum coil as the counter electrode, and an Ag/AgCl (1 M KCl) as the reference electrode, at RT. To identify the effect of the Ni/Fe ratio on the OER and HER catalytic activity of the NiFe-CNfS-CF electrode, the Ni/Fe ratio in the electrodeposition bath was varied and the synthesized

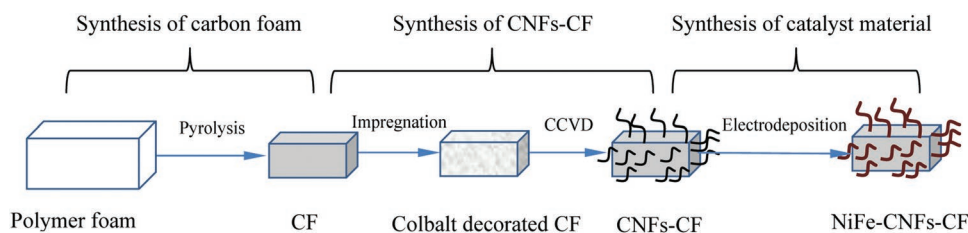
electrodes were tested. It was found that a 5/1 molar ratio of Ni²⁺ and Fe³⁺ yielded the NiFe-CNfS-CF electrode with the highest OER and also HER catalytic activity (Figure S2, Supporting Information). In detail, for the electrodeposition of the NiFe co-catalyst, the electrolyte bath contained 0.12 M of $\text{Ni}(\text{SO}_4)_2 \cdot 6\text{H}_2\text{O}$, 0.03 M of $\text{NiCl}_2 \cdot 6\text{H}_2\text{O}$, 0.06 M of H_3BO_3 , and 0.03 M of $\text{Fe}(\text{NO}_3)_3 \cdot 9\text{H}_2\text{O}$ in Milli-Q water. A similar plating bath, but without any iron source, was used in the synthesis of Ni-CNfS-CF and Ni-CF electrodes. The electrodeposition was performed at -1 V (vs Ag/AgCl) in 300 s, as suggested in the literature.^[30] After the electrodeposition, the electrodes were thoroughly rinsed with Milli-Q water and dried at 50 °C in air overnight. The shape of the prepared electrode is presented in Figure S1b in the Supporting Information.

Briefly, a simple procedure was used to synthesize the NiFe-CNfS-CF electrode involving three main steps: synthesis of CF, synthesis of CNfS-CF, and synthesis of catalyst material (Scheme 1).

The Bulk Density Determination: The bulk density of the CF materials: CF, CNfS-CF, and NiFe-CNfS-CF were calculated based on the respective mass and the geometry of the sample. The reported bulk density was determined by taking the average value of measured samples ($n = 7$). The standard error of the mean was estimated by dividing the standard deviation by the square root of the number of samples.

Characterization: SEM and EDS were carried out using a Zeiss Merlin FEG-SEM instrument. TEM measurements were performed on a JEOL JEM-1230 electron microscope operating at 80 kV. The HRTEM images of sample were collected with Talos L120C 120 kV (Thermo Fisher Scientific) equipped with LaB₆ electron source and 4k x 4k Ceta camera. Samples for TEM were suspended in ethanol (99.99%), sonicated (3 min), and deposited on a copper grid for analysis. TGA was conducted on a Mettler Toledo equipment (TGA/DSC 1LF) operated at a heating rate of 10 °C min⁻¹ up to 950 °C in air. The surface chemistry of the samples was examined using XPS. The photoelectron spectra were collected with a Kratos Axis Ultra DLD electron spectrometer using a monochromated Al K_α source operated at 120 W. An analyzer pass energy of 160 eV for acquiring wide spectra and a pass energy of 20 eV for individual photoelectron lines were used. The surface potential was stabilized by the spectrometer charge neutralization system. The binding energy scale was referenced to the C 1s line of aliphatic carbon, set at 285.0 eV, and the processing of the spectra was accomplished with the Kratos software. The concentration of nickel and iron elements in the electrolyte and the digested solution was determined using ICP-OES Spectrometer Optima 2000 DV (Perkin Elmer Instruments). The surface area measurements were carried out by N₂ sorption/desorption analysis (Tristar 3000 apparatus, Micromeritics Instrument Corp.). The surface area of samples was calculated by multipoint nitrogen gas sorptometry according to the BET principle. Before the analysis, the sample was degassed at 110 °C for 3 h in N₂ atmosphere. The XRD patterns were recorded in the 2θ angle range of 10°–70° with a scan rate of 1° min⁻¹ on a Panalytical X'Pert³ powder diffractometer using Cu K_α radiation.

Electrochemical Measurements: All electrochemical measurements were performed with a Modulab electrochemical system, ECS (Solartron Analytical, UK). For the three-electrode setup measurements in this study, the as-prepared CF electrodes, a platinum coil, and an Ag/AgCl (1 M KCl) were used as the working, counter, and reference electrodes, respectively. The 1 M KOH solution was used as the electrolyte in all electrocatalytic activity tests including the stability tests in this study. The OER experiments were performed in a single electrochemical cell.



Scheme 1. Schematic illustration of synthesis procedure of NiFe-CNfS-CF.

To eliminate the dissolution and re-deposition of platinum from the counter electrode as pointed out by Chen et al.,^[57] a two-compartment cell together with the Nafion N117 membrane was recruited for the HER experiments. To minimize the pH change in a long-term experiment in HER, the old electrolyte was partly replaced by new electrolyte every 24 h. Linear sweep voltammetry and CV were performed at a scan rate of 5 mV s⁻¹. Electrochemical impedance spectroscopy (EIS) experiments were performed at a defined over-potential in the frequency range 10⁵ to 0.1 Hz at 10 data points/decade with an applied alternating voltage of 10 mV. All measured potentials were calibrated to RHE using the Nernst equation: $E_{\text{RHE}} = E_{\text{Ag/AgCl}} + 0.235 + 0.059 \text{ pH}$ unless noted otherwise. The *iR*-corrected potential was obtained using the equation $E_{\text{iR-corrected}} = E - (95\%iR)$, where *i* represents the current, and *R* represents the ohmic resistance of the electrolyte, which was determined by the EIS experiments. The Tafel plots were derived from the polarization curves. The linear regions of the Tafel plots were fitted to the Tafel equation $\eta = \text{blog } j + a$ where η is the overpotential, *j* is the current density, and *b* is the Tafel slope.

Determination of the Double-Layer Capacitance: To evaluate the double layer capacitance values, *C_{dl}*, CVs were collected at different scan rates (*v*) (10, 20, 40, 60, 80, and 100 mV s⁻¹) by scanning from -0.1 to -0.18 V versus Ag/AgCl (except the CNFs-CF blank electrode which was performed that the potential of 0.05 to 0.15 V vs Ag/AgCl) which was in a non-Faradaic current region. The *C_{dl}* could be calculated using the following equation: $i_c = vC_{\text{dl}}$ where *i_c* is the capacitive current which could be identified based on the CVs run at -0.14 V versus Ag/AgCl (0.1 V vs Ag/AgCl for the CNFs-CF blank electrode).

Determination of Specific Current: The specific current (A g⁻¹) was calculated by dividing the measured current density *j* (mA cm⁻²) by the total weight of the electrode *M* (g cm⁻²)

$$\text{Specific current} = \frac{j}{1000 \times M} \quad (1)$$

$$j = \frac{I}{2 \times (L \times W)} \quad (2)$$

where *I* denotes the measured current (mA), *L* is the length (cm), and *W* is the width (cm) of the electrode.

Leaching Test-Determination of Catalyst in the Electrolyte: In general, the stability tests were performed in a single electrochemical cell which contained 7 mL of 1 M KOH electrolyte. After the test, the concentration of Ni and Fe in the electrolyte sample was measured by ICP-OES. Certified stock solutions of nickel and iron (1000 µg mL⁻¹) were used for the preparation of standard solutions and the construction of calibration curves.

Determination of the Catalyst Loading on the Sample: In a typical process, the sample was ground into a powder form and digested with concentrated nitric (60%). The mixture was sonicated in around 20 min and then digested at 125 °C overnight (reflux). The final clear solution was then diluted with an appropriate amount of Milli-Q water for the determination of nickel and iron using ICP-OES.

Determination of the Leaching Rate of Catalyst: To further study the rate of catalyst leaching in HER, two electrolyte samples were taken after 1 and 100 h during the stability test (at -150 mA cm⁻²) and measured separately using ICP-OES for their content of Ni and Fe. It should be noted that the electrolyte was renewed completely after the first sampling.

Faradaic Efficiency: The overall water-splitting reaction was performed in a gas-tight electrochemical cell with a small headspace volume. At first, the whole system was purged with nitrogen gas in 1 h to remove oxygen. During the reaction (at a constant *j* of 10 mA cm⁻²), the gas inflow (nitrogen) was maintained by a mass flow controller (Bronkhorst) at a specific flow rate, which is 80 and 160 times faster than the theoretical evolution rate of hydrogen and oxygen, respectively. The output gas was connected to a gas chromatography instrument (Varian 490-GC) equipped with a molecular sieve 5Å (M5A) column. For the long-term detection of evolved hydrogen and oxygen gas, the GC was set

to work in a continuous flow mode. Argon and helium gases were used as the carrier gas for the detection of hydrogen and oxygen, respectively. The faradaic efficiency was calculated from the theoretical volume (*V_{theo}*) which was derived from Faraday's law of water electrolysis and the evolved hydrogen/oxygen gas volume (*V_{exp}*) which was calculated based on the peak area of the evolved gas

$$\text{Faradaic efficiency} = \frac{V_{\text{exp}}}{V_{\text{theo}}} \% \quad (3)$$

$$V_{\text{theo}} = \frac{nRT}{P} \quad (4)$$

$$n = \frac{Q}{Fz} \quad (5)$$

where *n* denotes the moles of evolved hydrogen, *Q* is the charge passed, *F* is the Faraday constant, and *z* is the number of electrons transferred (*z* = 2 for hydrogen and 4 for oxygen). Ideal gas law was used to calculate the theoretical volume of hydrogen (at 293 K, 1 atm).

The calibration curve was built from a series of gas standards prepared from a stock gas mixture (5.007636% hydrogen in argon or 4.9930095% oxygen in helium, Air Liquide) which was then diluted to different concentrations using nitrogen gas. For the dilution, the gas volume was carefully controlled by two separate mass flow controllers (Bronkhorst), which were recalibrated for the use of nitrogen and the stock gas mixture.

Determination of TOF: The TOF of NiFe-CNTs/CF for HER/OER was calculated using the following formula

$$\text{TOF} = \frac{j \times A}{1000 \times (n \times F \times m)} \quad (6)$$

where *j* is the recorded current density (mA cm⁻²). For OER, *j_{OER}* was taken at the η_{OER} of 350 mV. For HER, *j_{HER}* was taken at the η_{HER} of 200 and 250 mV. *A* is the geometric area of the electrode. *n* is the number of electrons transferred in the reaction per unit of products (2 for H₂ and 4 for O₂). *F* is the Faraday's constant (96485 s A mol⁻¹) and *m* is the total number of moles of the Ni and Fe in the electrode. Assuming that all of the Ni and Fe atom on the electrode surface are active during the water-splitting reaction.

Supporting Information

Supporting Information is available from the Wiley Online Library or from the author.

Conflict of Interest

The authors declare no conflict of interest.

Data Availability Statement

The data that support the findings of this study are available in the supplementary material of this article.

Keywords

3D electrodes, carbon foams, lightweight electrodes, NiFe LDH, overall water splitting

Received: July 17, 2022
Revised: October 9, 2022
Published online:

- [1] E. Proietti, F. Jaouen, M. Lefèvre, N. Larouche, J. Tian, J. Herranz, J.-P. Dodelet, *Nat. Commun.* **2011**, *2*, 416.
- [2] J. A. Turner, *Science* **1999**, *285*, 687.
- [3] J. Tollefson, *Nature* **2010**, *464*, 1262.
- [4] K. Meier, *Int. J. Energy Environ. Eng.* **2014**, *5*, 104.
- [5] Á. Serna, F. Tadeo, *Int. J. Hydrogen Energy* **2014**, *39*, 1549.
- [6] J. Suntivich, K. J. May, H. A. Gasteiger, J. B. Goodenough, Y. Shao-Horn, *Science* **2011**, *334*, 1383.
- [7] D. Voiry, H. Yamaguchi, J. Li, R. Silva, D. C. B. Alves, T. Fujita, M. Chen, T. Asefah, V. B. Shenoy, G. Eda, M. Chhowalla, *Nat. Mater.* **2013**, *12*, 850.
- [8] A. Ursua, L. M. Gandia, P. Sanchis, *Proc. IEEE* **2011**, *100*, 410.
- [9] M. G. Walter, E. L. Warren, J. R. Mckone, S. W. Boettcher, Q. Mi, E. A. Santori, N. S. Lewis, *Chem. Rev.* **2010**, *110*, 6446.
- [10] Y. Lee, J. Suntivich, K. J. May, E. E. Perry, Y. Shao-Horn, *J. Phys. Chem. Lett.* **2012**, *3*, 399.
- [11] B. You, Y. Sun, *Acc. Chem. Res.* **2018**, *51*, 1571.
- [12] M. Gong, Y. Li, H. Wang, Y. Liang, J. Z. Wu, J. Zhou, J. Wang, T. Regier, F. Wei, H. Dai, *J. Am. Chem. Soc.* **2013**, *135*, 8452.
- [13] Y. E. Roginskaya, O. V. Morozova, E. N. Lubnin, Y. E. Ulitina, G. V. Lopukhova, S. Trasatti, *Langmuir* **1997**, *13*, 4621.
- [14] Z. Wang, S. Zeng, W. Liu, X. Wang, Q. Li, Z. Zhao, F. Geng, *ACS Appl. Mater. Interfaces* **2017**, *9*, 1488.
- [15] L. Yu, H. Zhou, J. Sun, F. Qin, F. Yu, J. Bao, Y. Yu, S. Chen, Z. Ren, *Energy Environ. Sci.* **2017**, *10*, 1820.
- [16] M. Kuang, Q. Wang, H. Ge, P. Han, Z. Gu, A. M. Al-Enizi, G. Zheng, *ACS Energy Lett.* **2017**, *2*, 2498.
- [17] J.-X. Feng, H. Xu, Y.-T. Dong, S.-H. Ye, Y.-X. Tong, G.-R. Li, *Angew. Chem., Int. Ed.* **2016**, *55*, 3694.
- [18] T. N. Pham, T. Sharifi, R. Sandström, W. Siljebo, A. Shchukarev, K. Kordas, T. Wågberg, J.-P. Mikkola, *Sci. Rep.* **2017**, *7*, 6112.
- [19] M. Cabán-Acevedo, M. L. Stone, J. R. Schmidt, J. G. Thomas, Q. Ding, H.-C. Chang, M.-L. Tsai, J.-H. He, S. Jin, *Nat. Mater.* **2015**, *14*, 1245.
- [20] N. Jiang, L. Bogoev, M. Popova, S. Gul, J. Yano, Y. Sun, *J. Mater. Chem. A* **2014**, *2*, 19407.
- [21] S. Czioska, J. Wang, X. Teng, Z. Chen, *ACS Sustainable Chem. Eng.* **2018**, *6*, 11877.
- [22] C. Tang, N. Cheng, Z. Pu, W. Xing, X. Sun, *Angew. Chem.* **2015**, *127*, 9483.
- [23] Yu Gu, S. Chen, J. Ren, Y. A Jia, C. Chen, S. Komarneni, D. Yang, X. Yao, *ACS Nano* **2018**, *12*, 245.
- [24] Z.-H. Xue, H. Su, Q.-Y. Yu, B. Zhang, H.-H. Wang, X.-H. Li, J.-S. Chen, *Adv. Energy Mater.* **2017**, *7*, 1602355.
- [25] P. Xiao, M. A. Sk, L. Thia, X. Ge, R. J. Lim, J.-Y. Wang, K. H. Lim, X. Wang, *Energy Environ. Sci.* **2014**, *7*, 2624.
- [26] A. B. Laursen, K. R. Patraju, M. J. Whitaker, M. Retuerto, T. Sarkar, N. Yao, K. V. Ramanujachary, M. Greenblatt, G. C. Dismukes, *Energy Environ. Sci.* **2015**, *8*, 1027.
- [27] B. H. R. Suryanto, Y. Wang, R. K. Hocking, W. Adamson, C. Zhao, *Nat. Commun.* **2019**, *10*, 5599.
- [28] Y. Hou, M. R. Lohe, J. Zhang, S. Liu, X. Zhuang, X. Feng, *Energy Environ. Sci.* **2016**, *9*, 478.
- [29] C. Tang, R. Zhang, W. Lu, L. He, X. Jiang, A. M. Asiri, X. Sun, *Adv. Mater.* **2017**, *29*, 1602441.
- [30] X. Lu, C. Zhao, *Nat. Commun.* **2015**, *6*, 6616.
- [31] C. Xiao, X. Zhang, S. Li, B. H. Suryanto, D. R. MacFarlane, *ACS Appl. Energy Mater.* **2018**, *1*, 986.
- [32] X. Hu, X. Tian, Y.-W. Lin, Z. Wang, *RSC Adv.* **2019**, *9*, 31563.
- [33] S. Zhao, J. Huang, Y. Liu, J. Shen, H. Wang, X. Yang, Y. Zhu, C. Li, *J. Mater. Chem. A* **2017**, *5*, 4207.
- [34] Z. Cai, X. Bu, P. Wang, W. Su, R. Wei, J. C. Ho, J. Yang, X. Wang, *J. Mater. Chem. A* **2019**, *7*, 21722.
- [35] D. Lehmhus, M. Vesenjak, S. De Schampheleire, T. Fiedler, *Materials* **2017**, *10*, 922.
- [36] M. F. Ashby, A. G. Evans, N. A. Fleck, L. J. Gibson, J. W. Hutchinson, H. N. G. Wadley, *Metal Foams: A Design Guide*, Elsevier, New York **2000**.
- [37] X. Han, X. Wu, Y. Deng, J. Liu, J. Lu, C. Zhong, W. Hu, *Adv. Energy Mater.* **2018**, *8*, 1800935.
- [38] X.-D. Wang, H.-Y. Chen, Y.-F. Xu, J.-F. Liao, B.-X. Chen, H.-S. Rao, D.-B. Kuang, C.-Y. Su, *J. Mater. Chem. A* **2017**, *5*, 7191.
- [39] J. Wang, H.-X. Zhong, Z.-L. Wang, F.-L. Meng, X.-B. Zhang, *ACS Nano* **2016**, *10*, 2342.
- [40] T. Sharifi, E. Gracia-Espino, X. Jia, R. Sandström, T. Wågberg, *ACS Appl. Mater. Interfaces* **2015**, *7*, 28148.
- [41] X. Wu, J. Yu, G. Yang, H. Liu, W. Zhou, Z. Shao, *Electrochim. Acta* **2018**, *286*, 47.
- [42] Y. Chen, J. Peng, W. Duan, G. He, Z. Tang, *ChemCatChem* **2019**, *11*, 5994.
- [43] S. Zhang, X. Yu, F. Yan, C. Li, X. Zhang, Y. Chen, *J. Mater. Chem. A* **2016**, *4*, 12046.
- [44] J. Zhang, H. Zhang, J. Wu, J. Zhang, in *Pem Fuel Cell Testing and Diagnosis*, Elsevier, New York **2013**, pp. 43–80.
- [45] C. Wang, F. Yang, Y. Cao, X. He, Y. Tang, Y. Li, *RSC Adv.* **2017**, *7*, 9567.
- [46] T. N. Pham, A. Samikannu, J. Kukkola, A.-R. Rautio, O. Pitkänen, A. Dombvari, G. S. Lorite, T. Sipola, G. Toth, M. Mohl, J.-P. Mikkola, K. Kordas, *Sci. Rep.* **2014**, *4*, 6933.
- [47] A. Ramos, I. Cameán, A. B. García, *Carbon* **2013**, *59*, 2.
- [48] S. Fu, C. Zhu, H. Li, D. Du, Y. Lin, *J. Mater. Chem. A* **2015**, *3*, 12718.
- [49] J. Xie, H. Qu, F. Lei, X. Peng, W. Liu, L. Gao, P. Hao, G. Cui, B. Tang, *J. Mater. Chem. A* **2018**, *6*, 16121.
- [50] J. Nie, M. Hong, X. Zhang, J. Huang, Q. Meng, C. Du, J. Chen, *Dalton Trans.* **2020**, *49*, 4896.
- [51] V. Torabinejad, M. Aliofkhaezrai, S. Assareh, M. H. Allahyarzadeh, A. S. Rouhaghdam, *J. Alloys Compd.* **2017**, *691*, 841.
- [52] J. Schreifels, *J. Catal.* **1980**, *65*, 195.
- [53] M. C. Biesinger, B. P. Payne, L. W. Lau, A. Gerson, R. S. C. Smart, *Surf. Interface Anal.* **2009**, *41*, 324.
- [54] A. N. Mansour, R. A. Brizzolara, *Surf. Sci. Spectra* **1996**, *4*, 357.
- [55] Y. Yi, G. Weinberg, M. Prenzel, M. Greiner, S. Heumann, S. Becker, R. Schlögl, *Catal. Today* **2017**, *295*, 32.
- [56] L. Ma, L. R. L. Ting, V. Molinari, C. Giordano, B. S. Yeo, *J. Mater. Chem. A* **2015**, *3*, 8361.
- [57] R. Chen, C. Yang, W. Cai, H.-Y. Wang, J. Miao, L. Zhang, S. Chen, B. Liu, *ACS Energy Lett.* **2017**, *2*, 1070.